MATERIALS SCIENCE

Unveiling the secret of ancient Maya masons: Biomimetic lime plasters with plant extracts

Carlos Rodriguez-Navarro*, Luis Monasterio-Guillot, Miguel Burgos-Ruiz, Encarnación Ruiz-Agudo, Kerstin Elert

Ancient Maya produced some of the most durable lime plasters on Earth, yet how this was achieved remains a secret. Here, we show that ancient Maya plasters from Copan (Honduras) include organics and have a calcite cement with meso-to-nanostructural features matching those of calcite biominerals (e.g., shells). To test the hypothesis that the organics could play a similar toughening role as (bio)macromolecules in calcium carbonate biominerals, we prepared plaster replicas adding polysaccharide-rich bark extracts from Copan's local trees following an ancient Maya building tradition. We show that the replicas display similar features as the organics-containing ancient Maya plasters and demonstrate that, as in biominerals, in both cases, their calcite cement includes inter- and intracrystalline organics that impart a marked plastic behavior and enhanced toughness while increasing weathering resistance. Apparently, the lime technology developed by ancient Maya, and likely other ancient civilizations that used natural organic additives to prepare lime plasters, fortuitously exploited a biomimetic route for improving carbonate binders performance.

INTRODUCTION

Lime plasters have been used for decorative and building purposes since the origin of pyrotechnology in the Levant ca. 10,000 to 12,000 BCE (*1*). Lime pyrotechnology involves calcination of carbonate rocks (e.g., limestones) to obtain quicklime (CaO), which is slaked to form $Ca(OH)_2$ (portlandite) that sets and hardens by reaction with atmospheric CO_2, forming a $CaCO_3$ cement (*2*). Pre-Columbian civilizations such as the Maya independently developed lime pyrotechnology (*2*–*3*), with first evidence for architectural use dating ca. 1100 BCE (*3*). They produced lime plasters, mortars, and stuccoes that display an unexpectedly good state of conservation (generally lacking typical damage features such as granular disintegration, fracturing and scaling, or loss of surface relief) despite >1200-year exposure to a deleterious hot and humid tropical environment (*4*). It is important to understand why these ancient Maya lime-based materials are so durable (in terms of resistance to both physical-mechanical and chemical weathering) not only to disclose the ancient Maya masons' technological achievements but also to design, using a reverse engineering approach, new lime-based plasters and mortars for their use in architectural heritage conservation and in modern, sustainable construction.

Much research has been dedicated to unveiling the secret that enabled Maya masons to produce these durable lime-based materials (*5*–*8*). This secret, however, remains elusive, although the beneficial use of natural organic additives has been suggested (*5*–*7*). In the Old World, plant extracts, sticky rice, fruit juices, oils, animal fats, and even blood or beer were often added to slaked lime to improve the properties of lime mortars and plasters (*9*–*11*). For instance, in his book *De Architectura*, Vitruvius indicated that oil (*Oleo subacta*) should be added to lime to make the lime mortar waterproof (*9*). In Mesoamerica, there is ample ethnohistoric, archaeological, and analytical evidence for the use of plant extracts by ancient Maya masons (*3*, *5*–*7*). Bishop Diego de Landa, in his 16th century chronicle *On the Things of Yucatan*, stated that "the higher part [of the Maya building] was a mortar roof, limewashed, and very strong, as it is currently made there with some sort of water coming from a tree bark." Organics (e.g., carbohydrates) found in Maya plasters and stuccoes match those present in the sap of barks from common trees in the Maya area (*7*–*8*), such as Chukum (*Havardia albicans*) (*5*) or Jiote (Chaká) (*Bursera simaruba*) (*6*). Following traditional plaster-making recipes inherited by modern Maya masons from their ancestors, researchers found that these additives improved the fresh-state properties (e.g., workability) of the plaster mix and reduced drying cracks, thus leading to a more compact set structure (*5*, *6*). However, these effects alone cannot fully explain why ancient Maya lime plasters are so durable, despite lacking [with a few exceptions (*12*)] hydraulic components such as ancient Roman mortars and concrete (*9*).

Here, we tested the hypothesis that natural organic additives, in addition to the abovementioned positive effects, could be adsorbed on and occluded in the calcite crystals formed after carbonation of slaked lime, strongly affecting the physical-chemical and mechanical properties of the set plaster in a similar way as in $CaCO_3$ biominerals (e.g., sea urchin spines or mollusk shells). In the latter, small amounts of inter- and intracrystalline (occluded) (bio)macromolecules such as proteins and polysaccharides (*13*–*19*) impart, via multiple strengthening/toughening mechanisms (*20*), physical-mechanical properties that far surpass those of their individual components (*21*). For this purpose, we analyzed ancient lime plasters from the Maya site of Copan and lime plaster replicas prepared, adding the polysaccharide-rich soluble extract of barks from Chukum and Jiote collected at the Copan site.

RESULTS

Analysis of ancient Maya plasters from Copan

We collected plaster samples from mid- to terminal-classic (540 to 850 CE) Maya structures at Copan. Figure 1 shows the different

Department of Mineralogy and Petrology, University of Granada, Fuentenueva s/n, 18002 Granada (Spain).
*Corresponding author. Email: carlosrn@ugr.es

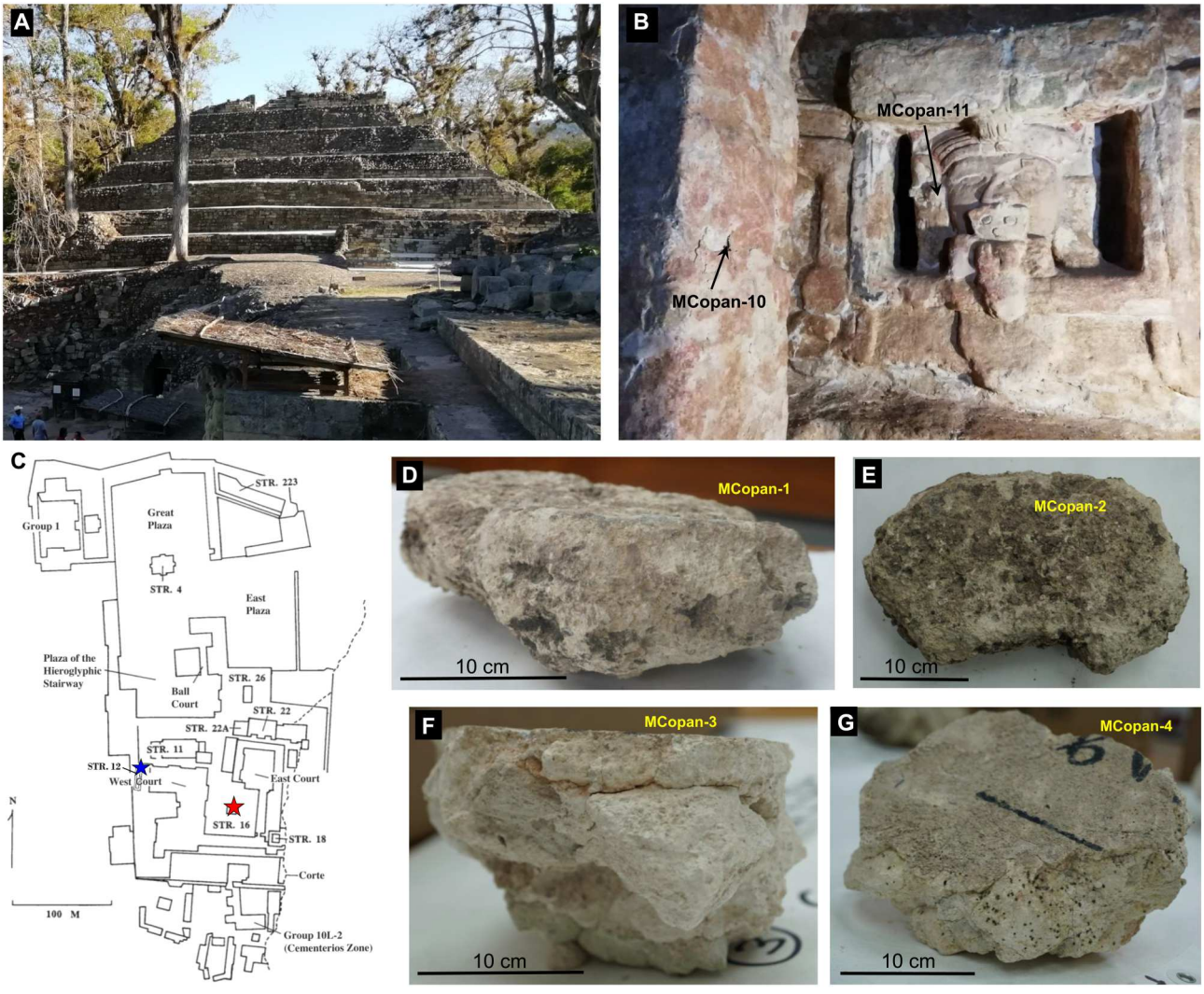

Fig. 1. Maya plasters from Copan archaeological site (Honduras). (**A**) General view of Structure 10L-16 (Late Classic building dedicated in 776 CE) (*22*). Within this structure is located substructure "Rosalila" (540 to 655 CE), the best example of a complete Classic temple in the Maya area, whose surface is decorated with pinkish lime plaster and stucco masks (**B**). Samples MCopan-10 and MCopan-11 were collected from the latter location, shown (marked with a red star) in the site map (**C**). Samples MCopan-1 (**D**) and MCopan-2 (**E**) corresponding to coarse lime plasters from the interior wall of the central room of Structure 12, ca. 700 CE [blue star in (C)]. Samples MCopan-3 (**F**) and MCopan-4 (**G**) corresponding to a fine two-layer plaster ("stucco") floor from the mid-Classic (500 to 700 CE) collected in tunnel 74 at Structure 10L-16. (C) adapted from (*22*) with permission from Springer Nature.

plaster samples and their location in the archaeological site. Table 1 details the samples' original location, age, mineralogy, and textural features. Samples MCopan-1 and MCopan-2 (fig. S1) are thick coarse plasters from a stucco-covered wall, MCopan-3 and MCopan-4 (fig. S2) are two-layer finer plasters from a floor, and MCopan-10 and MCopan-11 (figs. S3 and S4) correspond to pinkish, very fine lime plasters making up a wall and an adjacent stucco mask, respectively, on the exterior of Rosalila, the substructure entombed by Structure 10L-16 (*22*). Except for samples MCopan-1 and MCopan-2 that display a rough powdery surface, all other plaster samples show a good state of conservation. The ancient plasters include up to 95 weight percent (wt %) calcite according to x-ray diffraction (XRD) analysis and, with the exception of MCopan-1 and MCopan-2 that include relatively abundant (up to ~25 wt %) crushed local volcanic tuff stone aggregate (*23*), display a homogeneous texture, in some cases, presenting a minor fraction (<15 wt %) of tuff (with quartz, feldspars, mordenite zeolite, and silicate glass) as aggregate, observed with polarized light microscopy (PLM) (Table 1 and figs. S1 to S4). These observations are consistent with bulk chemical analysis (table S1) showing that the coarse plasters MCopan-1 and MCopan-2 have a relatively high SiO_2 and Al_2O_3 content (due to the presence of the tuff aggregate), whereas the rest of the samples have minor amounts of SiO_2 and Al_2O_3 and very high amounts of CaO, reflecting the presence of calcite as the main phase. Considering that the inclusion of crushed local Copan tuff stone as aggregate could lead to pozzolanic reactions upon mixing with slaked lime and impart a hydraulic character to the ancient Copan plasters (*9*, *12*), we performed detailed PLM and field-emission scanning electron microscopy (FESEM) imaging coupled with elemental energy-dispersive spectrometry (EDS)

Table 1. Mortar samples collected at the Maya site of Copan.

Sample	Description	Mineralogy (XRD analysis; wt %)	Texture	Notes
MCopan-1	Surface of a thick, coarse lime plaster ("Stucco") ~15 cm by 25 cm by 35 cm from an interior wall. Code #: 08/64/24. Location: Structure 12 (central room). Date: ca. 700 CE	Calcite (73) Quartz (10) Albite (9) Mordenite (8) ($CaCO_3$ content TG analysis; 77 ± 3 wt %)	Heterogeneous, dark matrix with aggregates of sparitic calcite (birefringent) in a micritic matrix.	Picture in Fig. 1D. PL M image and XRD pattern in fig. S1
MCopan-2	Interior of a thick, coarse lime plaster ("stucco") ~15 cm by 20 cm by 25 cm from an interior wall. Code #: 08/64/24. Location: Structure 12 (central room). Date: ca. 700 CE	Calcite (85) Quartz (9) Albite (1) Mordenite (5) ($CaCO_3$ content TG analysis; 82 ± 10 wt %)	Similar textural features as MCopan-1	Picture in Fig. 1E
MCopan-3	Surface layer from a two-layer white plaster ("stucco") floor ~15 cm by 19 cm by 23 cm in size from Tunnel 74. Code #: OP-41/2/1198 (CPN-28009). Location: Structure 10L-16 (tunnel). Date: ca. 500 to 700 CE	Calcite (95) Quartz (2) Mordenite (3) ($CaCO_3$ content TG analysis; 97 ± 1 wt %)	Homogeneous micritic matrix with few scattered tuff inclusions.	Picture in Fig. 1F
MCopan-4	Inner section of a two-layer white plaster ("stucco") floor ~14 cm by 18 cm by 20 cm in size from Tunnel 74. Code #: OP-41/2/11/96 (CPN-28009). Location: Structure 10L-16 (tunnel 74, lower level N29-N30). Date: ca. 500 to 700 CE	Calcite (94) Quartz (2) Mordenite (4) ($CaCO_3$ content TG analysis; 91 ± 1 wt %)	Coarse structure with micritic carbonate matrix and scattered aggregate (tuff) grains.	Picture in Fig. 1G. PL M image and XRD pattern in fig. S2
MCopan-10	Stucco (fine grained lime plaster) from the area on the left of the mask relief in the interior (tunnel) at "Rosalila" with a pale pinkish surface color. Location: Interior of Structure 10L-16. Date: Classic period (ca. CE 650)	Calcite (91) Quartz (5) Albite (4) Hematite (<1) ($CaCO_3$ content, TG analysis; 88 ± 1 wt %)	Fine grained dense calcite matrix. Scarce silicate aggregate. Two-layer coating: exterior reddish color (hematite).	Picture in Fig. 1B. PL M image and XRD pattern in fig. S3
MCopan-11	Surface plaster from the stucco mask in the tunnel of the interior of "Rosalila" with a pale pinkish color. Location: Interior of Structure 10L-16. Date: Classic period (ca. CE 650)	Calcite (85) Quartz (7) Albite (3) Mordenite (4) ($CaCO_3$ content, TG analysis; 87 ± 1 wt %)	Very fine grained (<1 mm), homogeneous plaster with scarce aggregate grains (silicates) with a thin (100 μm in thickness) red hematite layer.	Picture in Fig. 1B. PLM image and XRD pattern in fig. S4

analyses. Both PLM (fig. S5) and FESEM-EDS analyses (fig. S6) provide no clear evidence for Ca-Si-Al–rich reaction rims at the tuff-lime matrix interface, likely due to a poor pozzolanic reactivity of the Copan tuff aggregate. Although we cannot fully rule out the possibility that some hydraulic effect might exist in the plasters with the highest content of tuff aggregate (MCopan-1 and MCopan-2), it is very unlikely that pozzolanic reactions contributed to the high durability of the rest of the ancient plaster samples where the tuff aggregate content was minor.

FESEM analysis discloses that the calcitic binder has a nanogranular structure (Fig. 2A), most evident in the case of MCopan-3, MCopan-4, MCopan-10, and MCopan-11 plasters. These plasters include organics, as demonstrated by Fourier transform infrared spectroscopy (FTIR) analysis showing the C—H stretching bands of carbohydrates at 2840 and 2956 cm^{-1} and a weak band at 1630 to 1639 cm^{-1} corresponding to carboxylate groups (Fig. 2B and fig. S7) and by thermogravimetry/differential scanning calorimetry (TG/DSC) analysis (Fig. 2C and fig. S8) showing a mass loss of 0.64 ± 0.02 wt % and an associated exothermic band at 230° to 450°C, characteristic of the thermal decomposition in air of most organic molecules (*16*). No organics are detected by FTIR (Fig. 2B and fig. S7) or TG-DSC analysis (fig. S8) in Maya plaster samples MCopan-1 and MCopan-2, whose calcite crystals tend to display rhombohedral forms with smooth (non-nanogranular) faces (fig. S9), standard features of (abiotic) inorganic/geologic calcite (*15*, *24*). Transmission electron microcopy (TEM) with EDS microanalysis performed in scanning TEM (STEM) mode using a high-angle annular dark-field (HAADF) detector confirms that the ancient plasters with organics include highly pure (no Mg) calcite crystals (fig. S10) ~1 to 5 μm in size made up of aggregated nanoparticles (~30 to 100 nm in size) (Fig. 2D). They show single-crystal selected area electron diffraction (SAED) patterns with

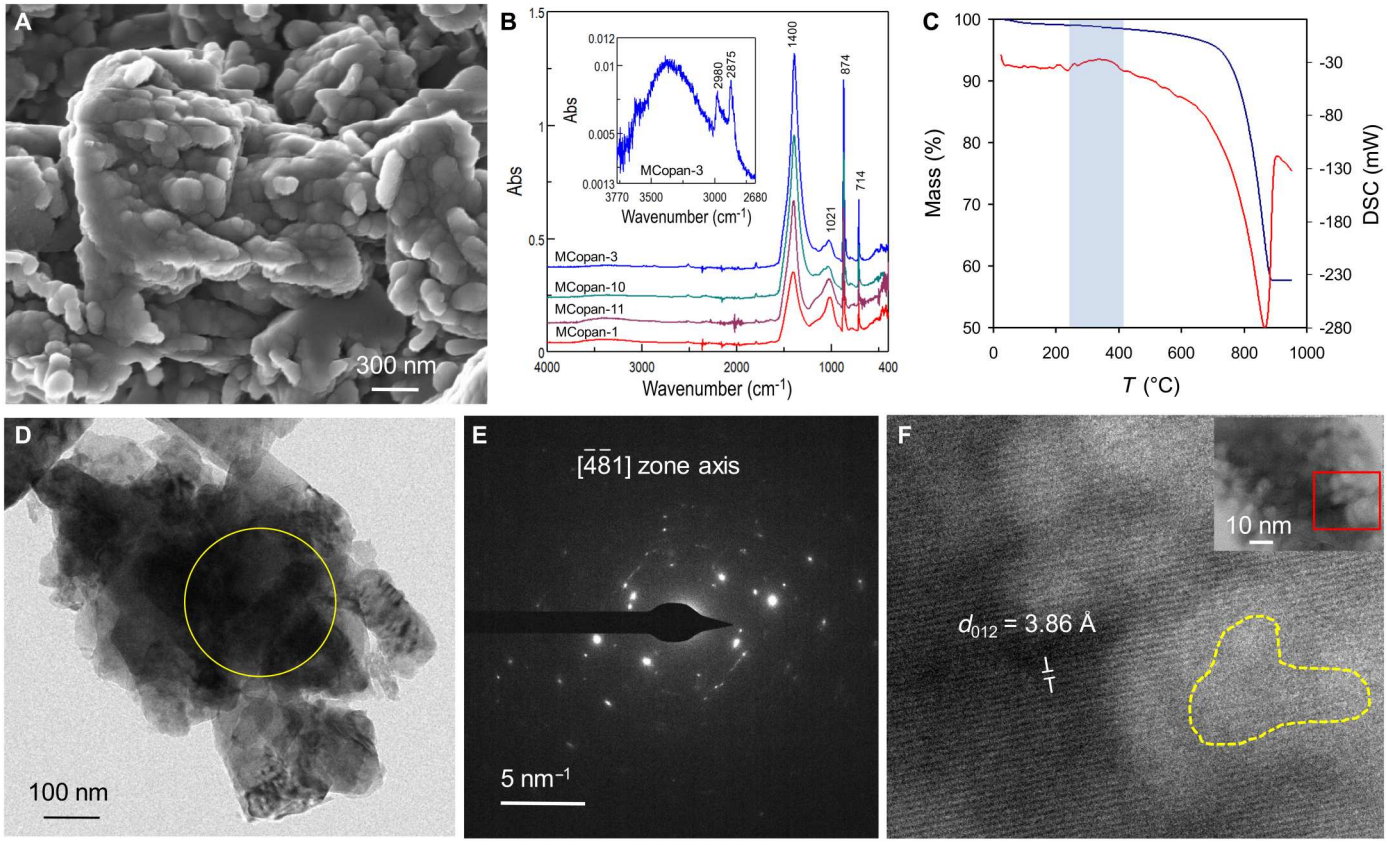

Fig. 2. Composition and microstructure of Copan plasters. (**A**) Representative FESEM image of the nanogranular structure of calcite cement in organics-including MCopan-4 plaster. (**B**) FTIR of Copan plasters showing intense bands corresponding to calcite (1400, 874, and 714 cm^{-1}) and a small broad band at 1021 cm^{-1} corresponding to silicate phases (aggregate). The inset shows a detail of the spectra of MCopan-3, which includes small amounts of polysaccharides as demonstrated by the C—H stretching bands at 2980 and 2875 cm^{-1}. The same bands are present in MCopan-4, MCopan-10, and MCopan-11, but not in MCopan-1 and MCopan-2. Abs, absorbance (arbitrary units). (**C**) TG (blue) and DSC (red) traces of sample MCopan-4 showing an exothermic band (shaded rectangle) corresponding to organics thermal decomposition in air. (**D**) TEM image of calcite crystal in MCopan-4 sample. (**E**) SAED pattern of the yellow circled area in (D). The spots display an angular spreading of ~4°. (**F**) HRTEM image of calcite in (D) (overall area in inset) showing lattice discontinuity (yellow dashed area) due to an amorphous inclusion.

slightly arced diffraction spots (angular spreading of ~4° to 6°) (Fig. 2E). These are standard features of calcite mesocrystals formed via a nonclassic oriented aggregation mechanism, typically involving amorphous calcium carbonate (ACC) nanoparticle precursors (*24*). High-resolution TEM (HRTEM) analysis shows low-contrast nanometer-size areas within individual calcite crystals with discontinuities in lattice fringes corresponding to an amorphous (organic) phase (Fig. 2F), similar to those observed in several $CaCO_3$ biominerals with occluded organics, such as sea urchin spines (*25*) and their biomimetics (*20*).

Plaster replicas including bark extracts

Having demonstrated that organics were present in the studied Maya lime plasters with features typical of calcite biominerals and their biomimetics (MCopan-3, MCopan-4, MCopan-10, and MCopan-11), we proceeded to test the hypothesis that the interaction of organics with the newly formed calcite cement resulted in the above-described biotic/biomimetic (nano)structural features. For this task and following the advice of local Maya-descendent masons, we extracted the sap of Chukum and Jiote bark collected at Copan (see Materials and Methods). The dry residue (0.5 wt %) of the aqueous extracts is made up of polysaccharides with abundant carboxylic functional groups (see details of the characterization in Supplementary Text and fig. S11), very similar to those of other polysaccharide-rich aqueous plant extracts used for the preparation of lime-based mortars and plasters by other ancient civilizations (*10*, *11*).

Quicklime was slaked in the absence and presence of Jiote or Chukum aqueous extract (see Materials and Methods and fig. S12 for details on the preparation and characterization of slaked limes) and allowed to set and carbonate for up to 2 months. FTIR and XRD analyses (figs. S12C and S13, A and B) show that carbonation follows a nonclassical path involving an ACC precursor, as it is systematically observed during carbonation in air of $Ca(OH)_2$ (*26*), and commonly occurs in $CaCO_3$ biominerals (*27*) and their biomimetics (*24*). The organic additives stabilize ACC and delay its transformation into calcite (*28*), resulting in lower portlandite to calcite conversion rates in additive-inclusive plasters as compared with the additive-free plaster (fig. S13C). Additive incorporation/adsorption into/onto calcite is confirmed by FTIR (fig. S13A) and TG/DSC (fig. S13D) analyses of carbonated replica plasters. FESEM and TEM analyses show that calcite crystals formed in the control

plaster display smooth surfaces (Fig. 3, A and B) and diffract as single crystals with no angular spreading (Fig. 3C). In contrast, calcite crystals formed in the presence of Chukum (Fig. 3, D to F) and Jiote (Fig. 3, G to I) extracts display similar nanogranular and mesocrystal features as those of the calcite binder in ancient Copan plasters including organics. HAADF-EDS analysis shows C enrichment on the calcite crystals surface (Fig. 3J), demonstrating adsorption of organics. HRTEM shows low-contrast amorphous areas

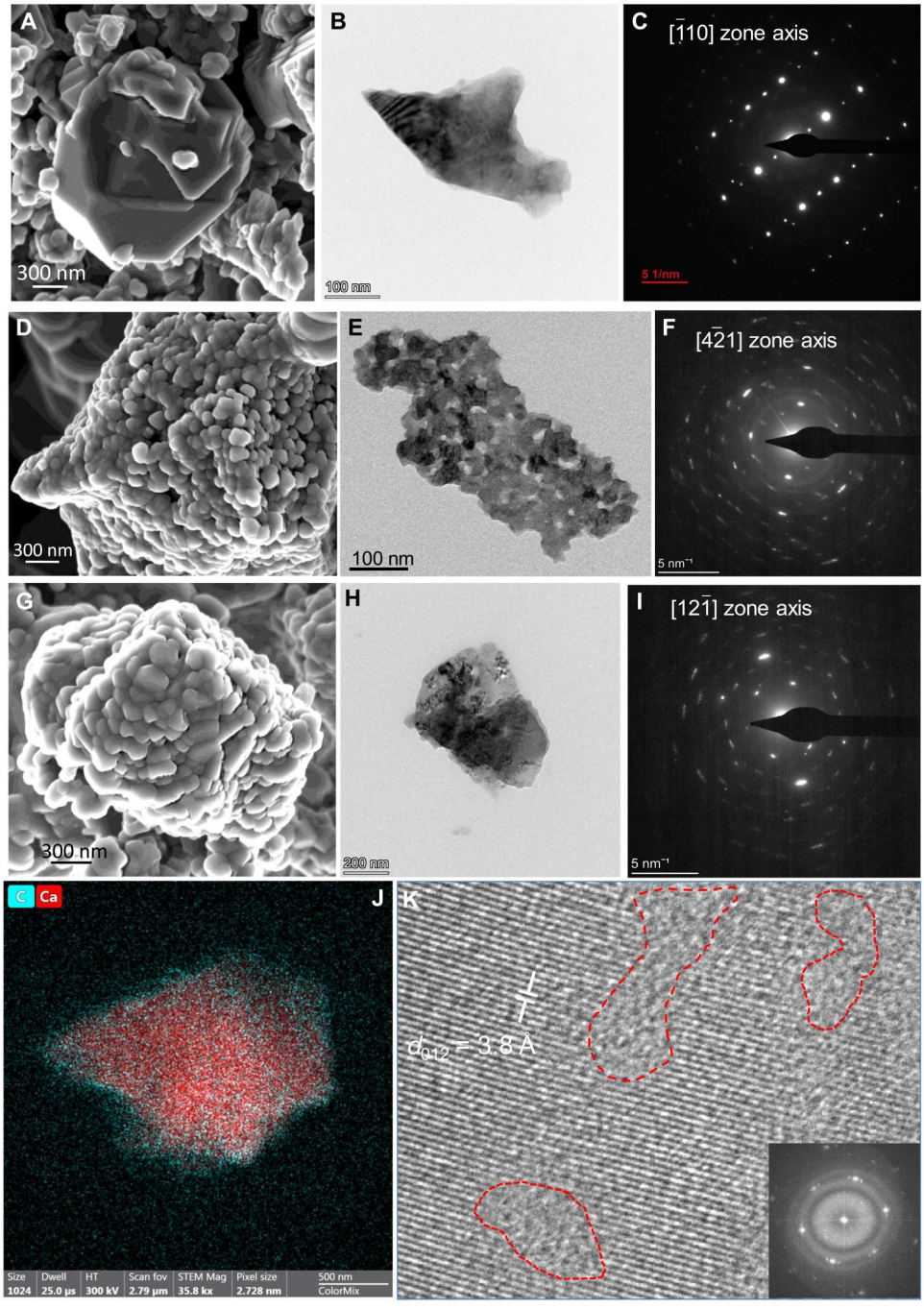

Fig. 3. Analysis of replica plasters. FESEM (**A**) of calcite in the control (additive-free) plaster (2-month carbonation) showing smooth rhombohedral faces and corresponding TEM (**B**) image and SAED pattern (**C**). FESEM (**D**) and TEM (**E**) images of granular (porous) aggregates of calcite in Chukum-including plaster (1-week carbonation) showing its single-crystal nature with angular spreading ~11° in the SAED pattern (**F**). FESEM (**G**) and TEM (**H**) images of calcite crystals formed in the presence of Jiote bark extract (2-month carbonation). Note the nanogranular structure (G) and the absence of porosity (H), likely due to calcite regrowth upon long term carbonation. (**I**) SAED pattern of calcite in (H) showing an angular spreading of ~9°. (**J**) HAADF-EDS mapping of calcite in Chukum plaster showing C (blue) concentration at the particle edges (2-month carbonation). (**K**) HRTEM of calcite in (H) showing amorphous regions corresponding to occluded organics (red dashed areas). Fast Fourier transform in inset.

within calcite crystals (Fig. 3K). Long-term exposure (~3 min) to the e-beam results in the transformation of the crystalline $CaCO_3$ areas into CaO nanocrystals, whereas no CaO crystals form in the amorphous areas (fig. S14). This suggests that the observed amorphous occlusions are organics, not ACC, which should readily transform into CaO crystals upon e-beam irradiation (*29*). It could be argued, however, that a mixture of ACC and organics could result in an amorphous material (i.e., amorphous CaO) upon e-beam–induced decomposition. This possibility can be ruled out on the basis of previous results showing the transformation of ACC including organics into crystalline CaO upon e-beam irradiation (*29*). However, we cannot rule out the possibility that other amorphous occlusions correspond to ACC or a mixture of ACC plus organics (*24*). Together, these results confirm the presence of both inter- and intracrystalline organics that modify the (nano)structure of the newly formed calcite crystals at multiple scales, reproducing the multiscale hierarchical, mesocrystal features observed in many $CaCO_3$ biominerals (*25*) and their biomimetics (*30*–*32*) that include inter- and intracrystalline (bio)macromolecules (*20*) and form after an ACC precursor (*24*, *27*). The fact that the micro- and nanostructural features of calcite cement in the replica plasters with polysaccharide-rich bark extracts match those of the calcite cement in ancient Maya plasters with organics, suggests, in agreement with the abovementioned archaeological, ethnohistoric, and analytical evidence, that the organics with FTIR spectral features of carbohydrates detected in the ancient Maya plaster samples from Copan are polysaccharide-rich plant extracts.

High-resolution synchrotron powder XRD analysis

To disclose possible macro- and microstrains in the calcite lattice of both the ancient Maya plasters and the replicas induced by the presence of intracrystalline (occluded) organics, a hallmark of calcite biominerals and their biomimetics (*15*–*18*, *20*, *32*, *33*), we performed high-resolution synchrotron powder XRD (HRXRD) analyses involving isochronous heating (annealing) (see Materials and Methods). As opposed to conventional XRD, synchrotron powder HRXRD analysis is accurate enough to detect lattice strains of 10^{-3} to 10^{-4} associated with intracrystalline organics (*15*–*18*).

Maya plasters including organics (MCopan-3, MCopan-4, MCopan-10, and MCopan-11) show a left shift in the 104, 001, and 110 Bragg peak positions (i.e., increase in *d*-spacing as compared with geologic calcite; fig. S15), which is absent (104 and 110 Braggs peaks) or very limited (001 Bragg peak) in organics-free samples (MCopan-1 and MCopan-2) (Fig. 4A and fig. S16). The variation of $\Delta c/c$ and $\Delta a/a$ (lattice strain fluctuations with respect to geologic calcite) with annealing T are graphically presented in Fig. 4 (B and C, respectively) (table S2 shows values of lattice parameter for each annealing T). These lattice strain fluctuations (up to 1.2×10^{-3}) are within the range reported for biogenic and biomimetic calcite (*15*–*19*, *33*). Copan plasters including organics show a systematic reduction in the *a* and *c* lattice parameters upon annealing, specially marked at $T > 200$°C, not observed in the MCopan-1 and MCopan-2 samples. Upon returning to room T, the *c* parameter increased, whereas the *a* parameter reached slightly lower values than those before annealing (table S2). This unexpected behavior seems to be a Poisson effect (i.e., contraction along the *a* axis results in expansion along the *c* axis) likely triggered by stress (and associated strain) relaxation upon heating and subsequent cooling. This effect is exclusive for lime plasters including organics. Lattice strain relaxation during annealing is due to the destruction of the occluded organics, a process that increases the number of interfaces resulting in increased microstrain and associated peak broadening (*17*, *18*). We observe a marked peak broadening due to crystallite size reduction and increased microstrain fluctuations upon annealing of organic-containing samples, not observed in MCopan-1 and MCopan-2 samples (table S3 and fig. S16). All these microstructural features are fingerprints for biogenic and biomimetic calcite with intracrystalline organic molecules (*16*, *18*, *32*), including carbohydrates (*33*). In agreement with HRTEM observations (Fig. 2F), our HRXRD results shown in Fig. 4 and fig. S16 unambiguously demonstrate that organics are present as intracrystalline occlusions in the calcite cement of the organic-containing historic plasters (MCopan-3, MCopan-4, MCopan-10, and MCopan-11). Our HRXRD analysis also confirms that samples MCopan-1 and MCopan-2 do not include occluded organics within the calcite crystals.

To confirm that organics are also occluded in calcite crystals of plaster replicas with bark extracts, we subjected them to HRXRD analysis. Bragg peaks of fully carbonated plaster replicas with organic additives show peak broadening and a left shift, especially for the 110 Bragg peaks (Fig. 4D) and larger *c* and *a* parameters as compared with geologic calcite (Fig. 4, B and C, and table S2). The fact that we also observe an expansion of the *a* lattice parameter in the additive-free control plaster is consistent with previous results (conventional XRD) showing lattice distortion in some additive-free lime plasters (*34*). However, a marked relaxation of the *c* lattice parameter occurs during annealing of replica plasters with organics, which is absent in the additive-free control (Fig. 4, B and C). This indicates that organics are occluded in calcite crystals of the former samples. Organics-including plasters have smaller domain size and larger microstrain fluctuation than additive-free plasters, and the former experienced a larger broadening (i.e., due to domain size reduction and microstrain increase) upon annealing than the latter (table S3). These results are fully consistent with the occlusion of organics in the replica plasters with bark extracts. We observe that the *a* lattice parameter experiences a large relaxation upon annealing in both the control and additive-including plasters, as shown by the marked right shift of the 110 Bragg peak, until it reaches the position of the 110 peak of reference geogenic calcite (fig. S17). As a result (Poisson effect), the *c* lattice parameter increases upon returning to room T after annealing, consistent with the left shift in the 001 Bragg peak (fig. S16). It is unclear why calcite in the replica plasters shows such a high lattice distortion along the *a* axis. It could be argued that this is due to a lower elastic modulus along such a direction as compared with the *c*-axis direction. However, the elastic modulus of calcite along the *a* axis is higher (91.6 GPa) than along the *c* axis (57.6 GPa) (*35*). A careful inspection of the variation in the *a* lattice parameter during annealing at $T \leq 200$°C shows an unexpected marked expansion, followed by relaxation, both in the control and additive-including plaster replicas (Fig. 4C). In biominerals, this has been associated with the presence of ACC transforming into calcite at such a T (*18*–*19*). It is reasonable to suggest that in the fully carbonated replica plasters with and without additives, there was a fraction of ACC (identified by XRD and FTIR; see above) occluded in calcite crystals, responsible for this odd behavior. However, it is unknown why such a possible ACC occlusion results in an anisotropic lattice distortion (i.e., maximum along

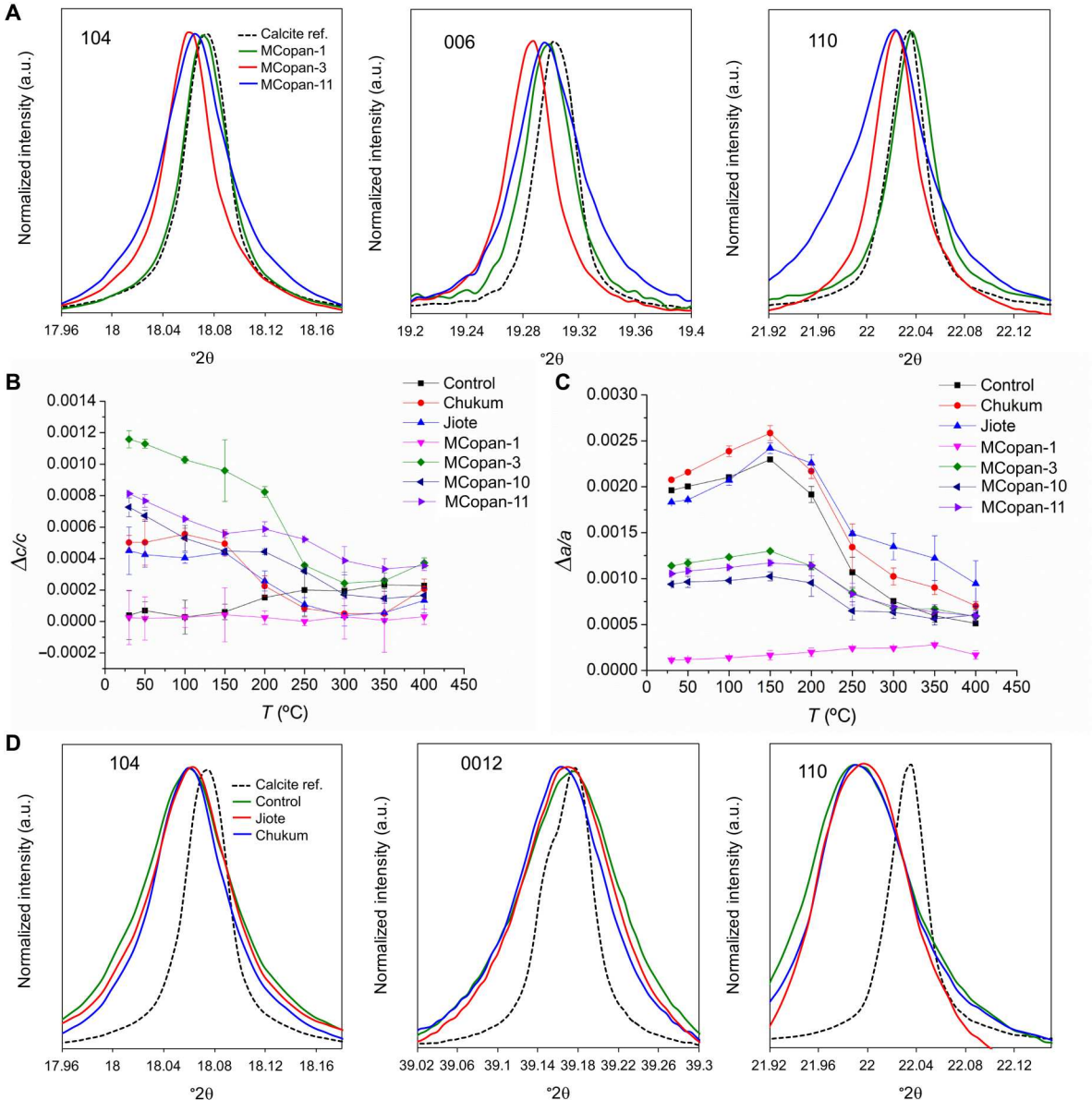

Fig. 4. Synchrotron powder HRXRD analysis of Maya plasters and replicas. (**A**) Profiles of 104, 006, and 110 Bragg peaks of calcite in selected ancient Maya plasters (MCopan-1 without organics and MCopan-3 and MCopan-11 with organics). The corresponding Bragg peaks of reference geogenic calcite (Iceland spar) are included. a.u., arbitrary units. (**B**) Variation in relative lattice strain along the *c* axis ($\Delta c/c$) with annealing *T* for selected ancient plasters and the three replica plasters. (**C**) Same as (B) for the *a* parameter. Error bars show SD (1σ). (**D**) Profiles of 104, 0012, and 110 Bragg peaks of calcite in the control and additive-including replica plasters (fully carbonated) as compared with reference geogenic calcite. X-ray wavelength of 0.9537249 Å.

the *a* axis) and how it affects occlusion of organics (*18*)—topics that warrant further research.

In summary, lattice distortions can help to identify pyrogenic calcite in plasters (*34*) and to disclose the presence of intracrystalline organics (*17*, *18*), which, as stated above, are fingerprints of calcite biominerals and their biomimetics. Another hallmark of carbonate biominerals and their biomimetics is the formation of an ACC precursor that includes organics (*25*, *27*). Upon transformation of ACC into crystalline calcite, these organics are partly expelled and partly occluded in the crystalline phase (*19*, *25*, *27*), which shows a nanogranular structure (*24*). We have shown the presence of ACC in the organics-including replica plasters undergoing carbonation, demonstrating that upon ACC-to-calcite transformation, the organics are occluded in calcite (i.e., HRTEM and HRXRD results), which displays a nanogranular structure. However, although we have also detected occluded organics in the calcite cement of the organics-including ancient Maya plasters, which show a nanogranular structure indicative of a nonclassical (biomimetic) growth via aggregation of precursor ACC nanoparticles (*24*), we have not identified ACC in these ancient plasters, likely because after more than 1200 years, any metastable ACC in these plasters transformed into calcite. Nonetheless, considering that carbonation of portlandite

systematically involves the formation of ACC before calcite (*26*), we can conclude that the formation of calcite with occluded organics both in the ancient Maya plasters and the replicas followed a biomimetic route.

Occlusion of organics in the calcite cement of ancient Maya plasters and replicas prepared with bark extracts must occur in two distinct ways: (i) Small molecules resulting from the alkaline degradation of polysaccharides in the soluble bark extract could replace carbonate groups in the calcite structure (*33*). We have previously shown that natural polysaccharides (nopal aqueous extract and pectin) undergo rapid alkaline hydrolysis via β-elimination at the highly alkaline pH of ~12.4 (and relatively high T) that was reached during lime slaking, resulting in their depolymerization into reducing sugars and, ultimately, (hydroxy)carboxylic acids (*11*). Those end-products are small molecules and could act as "solutes" within calcite crystals (*32*), their COO^- groups coherently replacing some of the carbonate groups in the calcite structure, as has been reported for acid monosaccharides (gluconic acid) (*33*) that cause lattice distortions (*17*, *33*) as observed here. (ii) Larger, nonfully degraded polysaccharide fractions could also be occluded (as demonstrated by HRTEM), contributing to the observed strain-related broadening. Note that foreign nanoparticle occlusion results in peak broadening due to microstrain contributions associated with the creation of intercrystallite boundaries acting as a source of inhomogeneous deformation fields but without necessarily contributing to macrostrain, i.e., lattice distortion (*17*, *18*, *32*).

Last, note that these intracrystalline organic (macro)molecules need to be occluded within calcite crystals during the formation of this carbonate phase, i.e., during the carbonation stage. Otherwise, the organics would just adsorb on the calcite cement of the lime plasters if they interact with the already formed calcite crystals, not contributing to the lattice distortions disclosed by our HRXRD analysis. This rules out the possibility that organics detected in historic Copan plasters and contributing to these lattice distortions are, for instance, polysaccharides [exopolymeric substances (EPSs)] from bacterial activity, which we have detected in these plasters and in carved tuff stone at Copan (*23*, *36*). Because fresh lime plasters undergoing carbonation have a highly alkaline pH of 12.4, it is very unlikely that any bacteria could survive and produce EPSs that might be incorporated in the newly formed calcite cement. Therefore, while it could be argued that (a fraction of) the organics detected here by FTIR and TG/DSC might correspond to EPSs from bacterial activity, the fact that we observed lattice distortion and relaxation during annealing by HRXRD unambiguously demonstrates that organics, i.e., polysaccharides from plant extracts, are present, occluded in the calcite crystals of the plasters, and were intentionally added during lime slaking and plaster preparation by ancient Maya masons.

Mechanical properties

To evaluate the effect of inter- and intracrystalline organics on the mechanical properties of the plasters' calcite, we performed nanoindentation analyses (see Materials and Methods). As expected (*37*), all plasters show a reduction in indentation (reduced) modulus E_r (fig. S18A) and indentation hardness H (fig. S18B) with increasing porosity (determined using mercury intrusion porosimetry; fig. S19). As a result, no clear differences in E_r and H among additive-free and additive-containing samples could be detected. Nonetheless, load displacement curves show that both ancient and replica plasters with organics display a marked plastic deformation during loading, with larger residual strain upon unloading than plasters without organics (Fig. 5A). We also observe pop-in (i.e., a sudden increase in displacement with no increase in load, under load-controlled indentation) associated with plastic yield (typically due to dislocation activation at the relatively low loads used here) (*38*). Pop-in occurs at a lower load in organic-free historic and replica plasters (P = 781 ± 229 μN, N = 10), as well as in geogenic calcite (P = 990 ± 421 μN, N = 4), than in organics-including plasters (P = 1124 ± 421 μN, N = 44). This might suggest that the latter plasters are more resistant to permanent deformation than the former ones. However, organics-including plasters have a lower value of yield stress τ (0.622 ± 0.111 GPa, N = 44) than organics-free samples (0.867 ± 0.244 GPa, N = 13). Moreover, the elasticity index, $I_E = H/E_r$, of organics-free plasters (0.065 ± 0.017, N = 40) is higher than that of organics-inclusive plasters (0.047 ± 0.007, N = 132), the latter value being within the range reported for

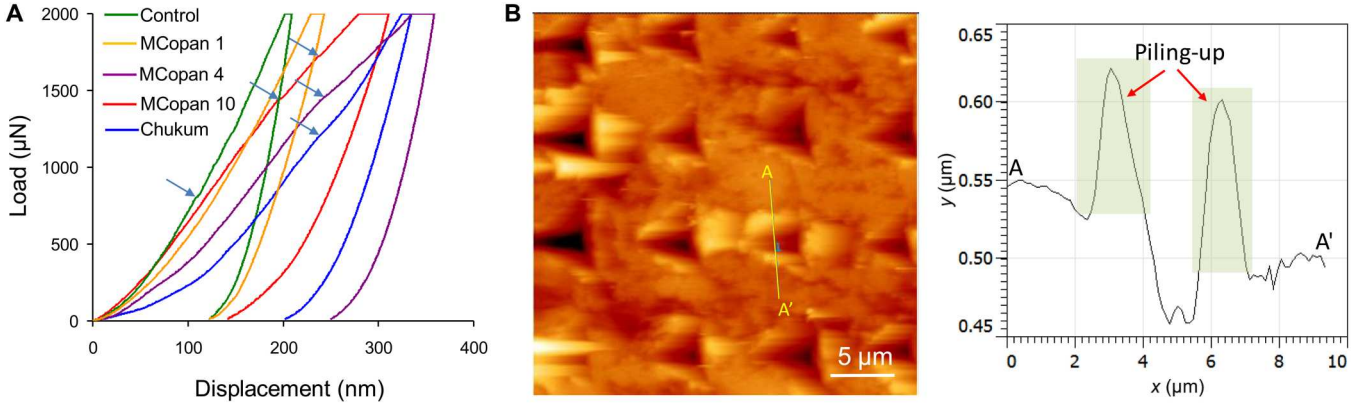

Fig. 5. Nanoindentation of lime plasters. (**A**) Representative load/displacement curves for historic (MCopan-1 without organics and MCopan-4 and MCopan-10 with organics) and replica plasters (organic-free control and Chukum-including plaster). Note the pop-ins (arrows) and the extensive plastic deformation in organics-including plasters shown by the increased displacement values at any applied load during the loading stage and the higher final displacement values after complete unloading. (**B**) Force microscopy image of indented area in MCopan-10. The AA′ height profile shows piling up at the two sides of the indented area but no cracks (depth-controlled indentation to 1000 nm, with maximum load of 18 mN). Replica plasters subjected to nanoindentation were fully carbonated (i.e., 2-month carbonation).

different biominerals (*39*). These results show that the organics make the plasters more plastic, which should prevent crack development. This is confirmed by force microscopy imaging after indentation showing piling-up without crack development (Fig. 5B). In contrast, fractures occur upon nanoindentation of organics-free calcite in the load range used here (*40*). Together, these results show that the organics induce a toughening effect, favoring plastic deformation and therefore hampering fracture-induced catastrophic failure (*20*, *32*). The nanogranular structure of the organic-containing plasters also enables toughening by the combined action of the granular rearrangement (under stress) and intergranular bridging by the organic phase (*41*). These effects should enable damage tolerance not only toward structural stresses but also to stresses associated with common physical weathering phenomena such as thermal expansion or in-pore salt crystallization pressure generation (*42*).

Resistance to chemical weathering

Lime plasters, especially in a hot and humid tropical environment, are subjected to chemical weathering (i.e., dissolution) (*43*). To evaluate the effect of the inter- and intracrystalline organics on the dissolution of the calcite cement in the plasters, we performed bulk dissolution tests (in MilliQ water, pH 6.5; see Materials and Methods) and measured continuously the time variation of conductivity, which provides information about the rate at which ions from $CaCO_3$ are released to the solution. The organics-free plasters, both ancient and replica ones, show a faster conductivity increase over time than the organics-including plasters (fig. S20), reflecting (qualitatively) that the dissolution rate of the former is higher than that of the latter. We also observe that the rate of conductivity increase in the replica plasters was higher than that of ancient Maya plasters. This is likely due to the fact that the former include metastable ACC (more soluble than calcite) and the latter include insoluble silicate phases as aggregate (i.e., the amount of carbonate binder per unit mass of plaster powder used in the dissolution tests would be smaller than in the replica plasters that include no aggregate). To gain further insights on how the organics reduced the dissolution rate of calcite, we performed in situ atomic force microscopy (AFM) experiments (see Materials and Methods). We first studied the growth of (104) calcite (Iceland spar crystals) in the absence and presence of Jiote and Chukum bark extracts. Right after injection of the growth solution, we observe step pinning following adsorption of the organic molecules at acute and obtuse steps and their subsequent occlusion (*44*). As a result, the standard shape of pyramidal growth hillocks at emerging dislocation is altered (Fig. 6, A to C). After 45 min, the organics induce a surface nanogranular structure (inset in Fig. 6C), similar to that of the plasters with organics (Figs. 2A and 3, D and E) and calcite biominerals (*24*), and arrest calcite growth. The observed arrest of calcite growth shows that the bark extracts are effective crystallization (growth) inhibitors, consistent with the lower carbonation rate of additive-inclusive plaster replicas observed here. Then, we evaluated how they affected calcite dissolution. In contact with deionized (DI) water (MilliQ), the bare calcite (without organic) dissolves via the formation of rhombohedral etch pits and steps retreat (Fig. 6D). In contrast, no step retreat or any sign of dissolution (in the time frame of our experiments) are observed in the case of calcite overgrown in the presence of organics (Fig. 6E). The observed effects would make the calcite binder in organics-inclusive plasters more resistant toward chemical weathering.

DISCUSSION

Our study of Classic Maya plasters from Copan and replicas made using the polysaccharide-rich aqueous extract from the bark of two common trees in the Maya area show that these organics are adsorbed on and occluded in the mesostructured calcite crystals making up the cement matrix of the plasters. These organics profoundly affect the physical-chemical and (nano)mechanical properties of the carbonate binder, rendering the plaster more resistant to physical and chemical weathering. The nanostructural features and properties of these modified plasters strongly resemble those of calcite biominerals and their biomimetics. Apparently, by serendipity, or more likely by trial and error, the Maya masons formulated biomimetic lime plasters with superior properties and durability. It is intriguing, however, that some studied ancient Copan plasters do not include organics, while others do. We can only hypothesize that for specific purposes where a more elaborate plaster or finishing surface was required, organics were added by ancient Maya masons (e.g., in substrates for mural painting, stucco masks, or floors), whereas in coarser plaster elements (i.e., MCopan-1 and MCopan-2), no organics were added (likely to make the process less complex and/or labor intensive).

Ultimately, our study helps to explain the improvement in the performance of lime mortars and plasters with natural organic additives developed not only by ancient Maya masons but also by other ancient civilizations (e.g., ancient Chinese sticky rice lime mortars). Last, the use of aqueous plant extracts could help to develop optimized and compatible lime-based mortars, plasters, and grouts for heritage conservation and modern sustainable construction. Our results pave the way for the design of novel biomimetic lime-based binders including natural or synthetic organics with specific functionalities or with well-known toughening effects such as those of the organics present in calcitic biominerals.

MATERIALS AND METHODS

Collection and analysis of Copan plasters

Lime plaster samples were collected at the Classic Maya center of Copan, a World Heritage Site (declared in 1992), located in the northwest of Honduras (36° 53′ 51.286" N; 95° 55' 33.934" W), close to the border with Guatemala. This city state was the premier site in the southeastern border of ancient Mesoamerica (*22*). Following the first written accounts of its existence by the Spaniard Diego García de Palacio back in 1576, the site was "rediscovered" in the 19th century, drawing international attention after the expedition by Stephens and Catherwood in 1841 (*22*). Since then, continuous archaeological research, site reconstruction, and conservation works have taken place, uncovering the magnificent structures of the so-called "Copan Main Group", also known as the Acropolis, including Structure 10L-26 that displays the famous Hieroglyphic Stairway, the longest written record of the ancient Maya world known to date (*22*). As a result of these extensive archaeological works, it is now possible to access the remains of lime plasters at the site, both in the different structures and in the tunnels opened within them, such as tunnel 74 accessing "Rosalila," the substructure enclosed in what is now Structure 10L-16 of the

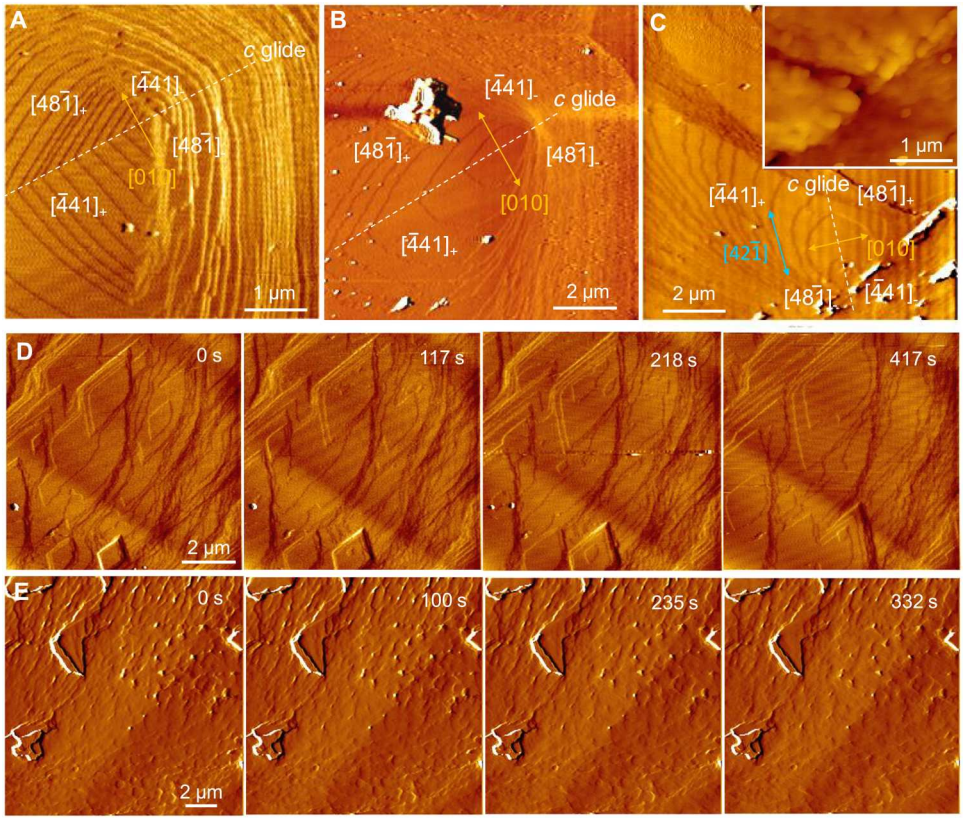

Fig. 6. AFM analysis of (104) calcite crystal growth and dissolution in the absence and presence of bark extracts using freshly cleaved Iceland spar. (**A**) Growth hillock developed on the (104) cleavage plane at an emerging screw dislocation in the absence of bark extract (deflection image, contact mode). The acute (−) and obtuse (+) steps, the [010] direction, and the *c*-glide plane are indicated. Changes in growth hillock shape (rounding of acute and obtuse steps) in the presence of Jiote (**B**) and Chukum (**C**) extracts (1.5 min after injection of the growth solution; deflection images). The inset in (C) shows a topographic (height) image of the final stage (after 45 min) of growth in the presence of Chukum extract. Note the nanogranular features of this overgrowth. (**D**) Time sequence of deflection images following injection of deionized (DI) water (1 ml min^{-1}) in the fluid cell at $t = 0$ s. Dissolution pits nucleate and enlarge via step retreat over time. (**E**) Time sequence of deflection images taken following growth in the presence of Chukum extract (45 min) and subsequent injection of DI water (1 ml min^{-1}) in the fluid cell at $t = 0$ s. No pits are nucleated nor is there any sign of dissolution over the recorded time span.

Copan Main Group (*22*), as well as the plaster collection at the Copan Museum of Sculptures. Note that, here, the term plaster is broadly used to refer to lime plasters, stuccoes, and mortars: i.e., lime-based structural (mortar), finishing (plaster), and decorative/sculptural (stucco) materials (*3*).

Samples of Copan plasters ($N = 6$) were collected from different areas of the archaeological site (Fig. 1 and Table 1). Plasters' textural features were studied using PLM (Olympus V) with transmitted and reflected light, using uncovered polished thin sections. The mineralogy was determined by XRD on a PANalytical X'Pert Pro equipped with Ni filter (measurement parameters: Cu Kα radiation λ = 1.5405 Å, 45 kV, 40 mA, 3° to 70° 2θ exploration range, steps of 0.001° 2θ, and goniometer speed of 0.01° 2θ s^{-1}). Powder samples were deposited on zero-background Si sample holders for analysis. Mineral phases were identified by comparison with International Centre for Diffraction Data powder spectra and quantified by means of the reference intensity ratio method. The bulk chemical composition of representative Copan plasters was determined by x-ray fluorescence (XRF) on a PANalytical Zetium. TG-DSC was performed on a Mettler-Toledo TGA/DSC1 to determine the amount of organics and carbonates. The historic plaster samples were also analyzed by attenuated total reflectance (ATR)–FTIR (Jasco) in the spectral range of 4000 to 400 cm^{-1} with a step size of 0.48 cm^{-1}. Additional microstructural and compositional features of Copan plaster samples were determined by FESEM (Zeiss AURIGA) equipped with EDS microanalysis. Samples were carbon-coated before FESEM observations. Ultrastructural features and detailed chemistry of phases in the historic samples were studied using TEM on a Titan and a Talos (FEI) with acceleration voltage of 300 and 200 kV, respectively. Both TEMs are equipped with HAADF detector for Z-contrast imaging and EDS for microanalysis (performed in STEM mode).

The porosity and pore size distribution of the plaster samples were determined using mercury intrusion porosimetry on an Autopore 9800 porosimeter (Micromeritics). Pieces with a mass of ~1 g were cut from the plaster samples and dried in an oven (24 hours at 80°C) before analysis.

Extraction and characterization of Chukum and Jiote aqueous extract

The sap of the barks of Chukum (*B. simaruba*) and Jiote (*H. albicans*) collected at Copan (March 2018) was extracted following

immersion of freshly collected bark pieces (~2 cm by 2 cm by 0.4 cm in size) in MilliQ water at room *T* (20°C) for 48 hours. The solid content after drying of the mucilaginous extract was, in both cases, ~5 g liter^{-1}. The ATR-FTIR spectra of the solid residues were very similar and show that the bark extracts of Chukum and Jiote are basically polysaccharides with abundant carboxylic functional groups (see details of the FTIR characterization in Supplementary Text and fig. S11A). Previous studies have shown that the aqueous extract of *B. simaruba* includes polysaccharides with abundant (poly)carboxylic acids, along with xylose and tannin (responsible for its reddish coloration) (*45*). Both Jiote and Chukum aqueous extracts have been reported to include galactose, arabinose, and rhamnose residues (*8*). TG/DSC analysis (in air atmosphere) of both plant extracts showed a broad exothermic band at ~200° to 400°C, with an associated mass loss corresponding to the thermal decomposition in air of the polysaccharides (fig. S11B).

Preparation and analysis of plaster replicas

Quicklime was prepared by calcination for 4 hours at 850°C (air-ventilated electric oven, Herotec) of ground calcitic marble (from Macael, Almeria, Spain). Note that this calcitic marble, used in historic buildings and statuary in southern Spain (e.g., the Alhambra Palaces), is highly pure (>99 wt % of $CaCO_3$). This ensured the absence of trace metals such as Mg that might affect the properties of the end-product calcitic cement in the plaster replicas (see below). Once calcined, the quicklime was slaked either in MilliQ water (control replica plaster) or MilliQ water with Chukum (Chukum replica plaster) or Jiote extract (Jiote replica plaster), having solid extract (5 g liter^{-1}) in either case. The water/oxide mass ratio was 3:1 (i.e., 66 g of H_2O and 33 g of CaO per batch). Slaking was performed under continuous stirring (magnetic stirrer module 801, Metrohm) in a 200-ml Teflon reactor coupled to a titration system (Titrino 905, Metrohm), controlled with Tiamo v2.5 software (Metrohm), and equipped with *T*, pH (glass electrode, Metrohm), and conductivity (856 conductivity module, Metrohm) probes. To avoid the possible carbonation of the highly alkaline solution (with initial pH ~13), a N_2 stream was continuously bubbled into the solution at a flow rate of 2.5 liter min^{-1}. Figure S11A shows the time evolution of *T*, demonstrating that the additives delay the slaking process, i.e., they increase the time to reach maximum *T*, acting as crystallization inhibitors (*11*). Following slaking, the calcium hydroxide dispersion (i.e., lime putty) was left to cool to room *T*, and aliquots were poured into plastic containers (petri dishes, 5 cm in diameter and 0.5 cm in height), to dry and carbonate for different periods of time under constant *T* (20° ± 2°C), partial pressure of CO_2 (~400 parts per million), and relative humidity (RH; 75 ± 5%) conditions. Samples were collected at predefined time intervals for up to 2 months (i.e., when 100% carbonation was achieved). Both the freshly slaked lime putties (freeze-dried, to preserve the original microstructure of the portlandite crystals and aggregates) and the lime plaster samples collected after different carbonation time were subjected to XRD, TG/DSC, ATR-FTIR, PLM, FESEM, and TEM-EDS analysis. In addition, in situ dynamic light scattering (DLS) analyses were performed at the end of the slaking process to measure the particle size distribution (PSD) of $Ca(OH)_2$ precipitates. Measurements were conducted at a scattering angle of 180° using a Microtrac NANO-flex particle size analyzer equipped with a diode laser (λ = 780 nm, 5 mW) and a 1-m-long flexible measuring probe (8 mm in diameter) with sapphire window as the sample interface. Scattering was measured with an acquisition time of 30 s, performing at least 120 consecutive measurements. PSDs were computed with the Microtrac FLEX application software package (v.11.1.0.2). N_2 sorption isotherms of (freeze-dried powder) slaked limes were performed at 77 K on a Tristar 3000 equipment (Micromeritics) to obtain their Brunauer-Emmett-Teller–specific surface area values. Figure S6 (B to G) shows the results of the DLS, FTIR, FESEM, and TEM-EDS analysis of the freshly prepared lime putties with and without bark extracts.

Similar analyses (with the exception of in situ DLS) were performed on the replica plasters subjected to different carbonation periods. In addition, we also performed XRD analysis of plaster samples collected at different periods of time (1 day up to 2 months) before and after oven heating at 350°C for 2 hours. This treatment reveals whether ACC is present within a carbonating lime plaster. ACC converts into calcite at such *T*, and this leads to an increase in the intensity of the Bragg peaks of calcite (*46*). In our case, and in agreement with previous studies of the carbonation of $Ca(OH)_2$ particles (*26*, *47*), ACC was present as a precursor to calcite (at any sampled carbonation time). The formation of ACC as a precursor to calcite was confirmed by FTIR analysis showing a broad σ_3 band at 1400 cm^{-1} and the absence of the calcite σ_4 band at 713 cm^{-1} in pastes carbonated for <24 hours (*27*).

Synchrotron HRXRD

HRXRD analysis was performed at beamline BL04-MSPD of the ALBA synchrotron (Barcelona, Spain). The wavelength, 0.9537249 Å (13 keV), was selected with a double-crystal Si (111) monochromator and determined by using Si640d National Institute of Standards and Technology standard (a = 5.43123 Å). The beam line is equipped with a high-throughput position-sensitive detector MYTHEN especially suited for time-resolved experiments. Borosilicate glass capillaries of 0.7 mm in diameter were loaded with powder samples and rotated during data collection to improve diffracting particle statistics. Isochronous annealing (10°C min^{-1}; 30-s stabilization time at target *T*, tolerance ± 5°C) was performed using a Cyberstar hot gas blower with a Eurotherm *T* controller (Eurotherm, Worthing, UK), collecting diffraction data each 50°C during the heating ramps (50° to 400°C). Once the maximum *T* was reached, the samples were cooled to room *T*, and a final measurement was taken. The data acquisition time was 5 min per pattern, with two iteration per measurement to obtain a good signal-to-noise ratio over the 3° to 95° 2θ angular range. To calibrate the equipment and reduce possible shifts during experimental analysis, NAC standard ($Na_2Al_2Ca_3F_{14}$) was used (for each *T* ramp sample point). An instrumental resolution factor analysis was performed using NAC. Under these data acquisition conditions, the angular resolution was 0.006° full width at half maximum (FWHM).

The Rietveld refinement method (*48*) was used to extract lattice parameters of $CaCO_3$, matching the experimental diffraction peaks with those included in Markgraf and Reeder (*49*), using Fullprof software (*50*). Optical quality (highly pure) geologic calcite (Iceland spar, from Chihuahua, Mexico) was used as standard to compare XRD data from replica and archaeological lime plasters and to parameterize thermal expansion over the selected experimental *T* range (fig. S15A).

To investigate the microstructural variations due to organic (macro)molecule incorporation in the calcite structure, the Thompson-Cox-Hastings pseudo-Voigt function was used to fit the profile

of the experimental diffraction patterns. Microstrain fluctuations (σ) were calculated using the Williamson-Hall plot method (*51*) for three-order Bragg reflections of (*h*0*l*), (*hh*0), and (00*l*) crystallographic planes. Fifteen refinement cycles were performed to ensure reproducibility of each analysis, selecting a Goodness of Fit of <9. These parameters reduce the discrepancy between experimental and fitting values in a normal statistical distribution. Figure S15A shows the variation with *T* of *a* and *c* lattice parameter for geologic calcite, and fig. S15B shows the 104, 110, and 006 Bragg peaks of reference geologic calcite before and after annealing. No changes in Bragg peak position or broadening (FWHM) were observed after annealing, i.e., after returning to room *T* following heating up to 400°C. These results show that the selected geogenic calcite is a proper reference to compare the results of the plasters' HRXRD analysis.

Nanoindentation

Nanoindentation of historic and replica plasters was performed using a Bruker Hysitron TI Premier nanoindenter, equipped with a diamond Berkovich tip (with trigonal pyramidal shape, semiangle = 65.3°) and scanning probe microscopy. Before testing, samples were embedded in epoxy resin (under vacuum), cut using a diamond saw, and prepared either as (uncovered) polished thin sections (~30 μm in thickness) mounted on glass slides or as monolithic epoxy cylinders (2.5 cm in diameter and 1 cm in height), with the upper circular face polished, exposing the embedded sample. Polishing was performed using γ-Al_2O_3 powder, with different sizes down to 100 nm to minimize surface roughness. Note that we have focused on the analysis of the mechanical properties at the micro/nanoscale rather than at the macroscale. Because of the high historical value of these archaeological plaster samples, we could not bring to our laboratory samples large enough to perform macroscale mechanical tests. It should be mentioned, however, that it has been reported that the mechanical properties determined at the micro/nanoscale are fully relevant at the macroscale (*52*).

Nanoindentation measurements were performed under *T*- and RH-controlled conditions (20°C, 40% RH). Considering the heterogeneous and porous nature of the studied plasters and to obtain representative results, we performed more than 200 nanoindentations (a minimum of 25 per tested sample) using grids of either 3 × 3 or 4 × 4 indenters (spaced at 9 μm both in the lateral and vertical directions) per sampled area. Two modes for indentation were implemented: (i) load control and (ii) displacement control. In the former case, a maximum load of 2000 μN was selected to ensure that the indentation depth was notably larger than any surface feature (roughness), whereas, for the latter case, a maximum displacement of 1000 nm was selected to disclose whether a much larger indentation depth than in the previous case affected the results. In general, more consistent results, in terms of reduced modulus (E_r) and indentation hardness (*H*), were obtained using load-control measurements, whereas no marked variations in E_r and *H* were observed when comparing load- or displacement-control runs (i.e., variations in these parameters were within error).

Calibration of the indenter tip using polydimethylsiloxane and fused quartz standards was performed before and during sample analysis. In addition, nanoindentation was systematically performed on the epoxy area of each sample to evaluate whether measured spots within the plasters corresponded to the calcite binder or to pore areas (filled with the resin). Load displacement curves showing the standard features and E_r and *H* values of the epoxy resin (E_r = 4.5 ± 0.7 GPa and *H* = 0.25 ± 0.04 GPa) were discarded. Similarly, for the calculation of E_r and *H* of plasters, load displacement curves showing nonstandard features (i.e., departing from the Hertzian behavior, such as displacement bursts, also known as pop-in) (*38*) were discarded. Last, 149 valid load displacement curves were obtained for the eight samples subjected to nanoindentation analysis (historic plasters: MCopan-1, MCopan-3, MCopan-4, MCopan-10, and MCopan-11; replicas: Control, Jiote, and Chukum).

Indentation was performed at a loading/unloading rate of 200 μN s^{-1} with a holding time of 10 s (to allow for the material to reach a stabilized state). The Oliver and Pharr (*52*) model was used to determine E_r and *H*. The reduced modulus was calculated from the slope of the unloading curve [contact stiffness, $S = (dP/dh)_{h_{max}}$, where *P* is the load and *h* and h_{max} are the indentation depth at a given unloading point and at maximum P_{max}, respectively] using the following equation

$$E_r = \frac{\sqrt{\pi}}{2\beta}\frac{S}{\sqrt{A}} \quad (1)$$

where β is a constant that depends on the geometry of the indenter (β = 1.034 for a Berkovich indenter) and *A* is the projected contact area of the indenter tip, which is given by the indentation depth *h*, knowing the geometry of the indenter.

The reduced modulus depends on the Young's modulus and Poisson ratio of the indented material (*E* and ν) and the indenter (E_i and ν_i) as given by

$$\frac{1}{E_r} = \frac{(1-\nu^2)}{E}\frac{(1-\nu_i^2)}{E_i} \quad (2)$$

Equation 2 enables the determination of *E* for the indented material if its Poisson ratio is known, as the modulus and Poisson ratio of the diamond indenter are known (E_i = 1141 GPa, ν_i = 0.07). In our case, as the value of Poisson ratio of calcite changes with [*hkl*] direction (*40*), we did not attempt to calculate *E* values, but rather, for comparison purposes, we systematically used E_r values.

H values were determined using the following equation (for a Berkovich indenter)

$$H = \frac{P_{max}}{A} \quad (3)$$

As a reference, the values of E_r and *H* of geogenic calcite [slabs of ~10 mm by 10 mm by 3 mm cut along the (104) cleavage plane of highly pure, optical quality Iceland Spar crystals from Chihuahua, Mexico] were determined under the same measurement conditions as indicated above. A 4 × 4 indentation grid was used on the (104) face of these calcite crystals. Note that the obtained average values of E_r [52.6 ± 0.95 GPa; yielding a value of Young's modulus *E* of 61 ± 1 GPa using Eq. 2 and assuming that the Poisson ratio of calcite is 0.3 (*53*)] and *H* (2.17 ± 0.07 GPa) are slightly below those commonly reported for synthetic or geogenic calcite [e.g., *E* of 88 GPa and *H* of 2.54 GPa (*32*, *40*)]. However, these obtained E_r and *H* values are within the range of values reported by Merkel *et al.* (*53*) and nearly match those recently reported by Deng *et al.* (*54*), who claim that these relatively small values were likely the result of using a new Berkovich tip, as it is also our case.

Considering that both the historic and replica plasters were porous, we used different models to fit the variation of E_r with fractional porosity, ø. Tested models included the Voight, the Ramachrisna and Arunachalam, and the Pabst-Gregrovà models (*37*), as well as the models for overlapping spheres, ellipsoidal pores, overlapping spherical pores, and overlapping ellipsoidal pores by Roberts and Garboczi (*55*). The best fit was obtained using the model for overlapping ellipsoidal pores (fig. S18A)

$$\frac{E_r}{E_{r0}} = (1 - \phi)^{2.25} \quad (4)$$

where E_{r0} is the reduced modulus of the nonporous material (i.e., geogenic calcite). We also considered these models to fit the variation of H with ø. However, none of the abovementioned models yielded a good fit. The best fit was obtained using a linear regression (fig. S18B).

We calculated the radius R of the tip of our Berkovich indenter using the Hertz contact model (*56*), which gives the following relationship between the applied load P and the resulting indentation depth h

$$P = \frac{4}{3} E_r \sqrt{R} h^{\frac{3}{2}} \quad (5)$$

To calculate R using Eq. 5, we used experimental E_r values obtained using the reference geogenic calcite, yielding an average R value of 115 ± 5 nm. Then, we used this value to calculate the yield stress, τ, marking the elastic to elastoplastic transition during indentation of the plaster samples. This transition is shown by a sudden burst in the displacement of the load/displacement curves, i.e., pop-in (*38*). For this task, we used the analytical solution given by Hertz that enables the calculation of the induced shear stress in the material under the spherical tip of the indenter (*56*)

$$\tau = \left(\frac{6 P_p {E_r}^2}{1.6^3 \pi^3 R^2} \right)^{\frac{1}{3}} \quad (6)$$

where P_p is the load at which the first pop-in takes place, marking the onset of plastic deformation.

Determination of bulk dissolution rates of calcite present in replica plasters

The dissolution rate in water (MilliQ) of calcite present in the replica plasters with and without organic additives, as well as in ancient Copan plaster without (MCopan-1) and with organics (MCopan-4), was determined using a Titrino 905 manufactured by Methrom, which allows continuous monitoring of pH, T, and conductivity. Plaster replicas (fully carbonated for 2 months) and ancient Maya plasters were grinded in an agata mortar. Powder samples were then sieved to collect particles with grain size ranging from 50 to 100 μm. A mass of 0.1 g of the resulting powder was dispersed in 100 ml of MilliQ water and measurement of the above listed parameters started. The dispersion was stirred using a magnetic stirrer (200 rpm) during data collection. Once the values of conductivity started to stabilize, the run was stopped. Here, the variation (increase) of conductivity with time is considered as a proxy for the (qualitative) evaluation of the dissolution rate of $CaCO_3$ present in the plasters.

In situ AFM

To gain further insights on the effect of inter- and intracrystalline organics on the dissolution of calcite cement in the plasters at the nanoscale, we performed in situ AFM analyses of the growth and dissolution of {104} calcite surfaces in the presence and absence of Jiote and Chukum bark extracts. We used a Multimode v.8 AFM equipped with a fluid cell (Bruker) working in contact mode under ambient conditions (T = 23°C). AFM images were collected using nitride-coated silicon tips (Bruker, tip model SCANASYST-FLUID) with spring constant of 0.7 N m^{-1}. Images were collected using NanoScope 10.0 software and analyzed using the NanoScope Analysis package (Version 3.00). Freshly cleaved optical quality Iceland spar crystals (~3 mm by 3 mm by 1 mm in size, from Chihuahua, Mexico) were used as substrates. Before each growth experiment, double-DI water (resistivity of >18 milliohm cm^{-1}) was passed over the crystal to clean the cleaved surface and to adjust the AFM parameters. Growth solutions flowed semicontinuously at an average rate of 60 ml $hour^{-1}$ from a syringe coupled to the O-ring–sealed fluid cell containing the sample crystal. Calcite growth solutions were prepared by adding calculated volumes of $CaCl_2$ and Na_2CO_3 from 1 M stock solutions, to obtain a saturation index with respect to calcite, $SI_{calcite}$, of 0.84 [SI = log(IAP/K_{sp}), where IAP is the ion activity product and K_{sp} is the solubility product of a relevant phase, in our case calcite]. The precision of added volumes is ±1 μl. Stock solutions were prepared by dissolving reagent-grade sodium carbonate (Na_2CO_3; Sigma-Aldrich) and calcium chloride ($CaCl_2 \cdot 2H_2O$; Sigma-Aldrich) into double-DI water. Growth in the presence of organics was performed adding 0.01 wt % of Chukum or Jiote bark extract to the growth solution. We primarily targeted areas where rhombohedral growth hillocks appeared (i.e., growth associated with steps spreading at emerging screw dislocations). Once a growth hillock was observed, the growth solution with the organic additive was injected in the flow cell, and images were collected. In addition, surfaces grown in the presence of the organic additive were scanned at 2 Hz in tapping mode for qualitative nanomechanical mapping using the Peak Force QNM method. Last, dissolution experiments were performed injecting MilliQ water in the fluid cell while continuously collecting images of the scanned area, both using crystals previously overgrown in the presence and in the absence of the additives.

Supplementary Materials

This PDF file includes:

Supplementary Text
Figs. S1 to S20
Tables S1 to S3
References

REFERENCES AND NOTES

1. W. D. Kingery, P. B. Vandiver, M. Prickett, The beginnings of pyrotechnology, part II: Production and use of lime and gypsum plaster in the Pre-Pottery Neolithic Near East. *J. Field Archaeol.* **15**, 219–243 (1988).
2. R. S. Boynton, *Chemistry and Technology of Lime and Limestone* (Wiley, 1980).
3. E. F. Hansen, *Ancient Maya Burnt-Lime Technology: Cultural Implications of Technological Styles* (University of California, Los Angeles, 2000).
4. D. Hyman, *Precolumbian Cements: A Study of the Calcareous Cements in Prehispanic Mesoamerican Building Construction* (John Hopkins University Press, 1970)
5. E. H. Morris, J. Charlot, A. A. Morris, *The Temple of the Warriors at Chichen Itza, Yucatan* (Carnegie Institution, 1931).

6. E. R. Littmann, Ancient Mesoamerican mortars, plasters, and stuccos: The use of bark extracts in lime plasters. *Am. Antiquity* **25**, 593–597 (1960).
7. D. Magaloni, R. Pancella, Y. Fruh, J. Cañetas, V. Castaño, Studies on the Mayan mortars technique. *MRS Online Proc. Lib.* **352**, 483 (1995).
8. N. Guasch-Ferré, J. L. Prada Pérez, M. L. V. de Agredos Pascual, L. Osete-Cortina, M. T. Doménech-Carbó, Polysaccharide remains in Maya mural paintings: Is it an evidence of the use of plant gums as binding medium of pigments and additive in the mortar? *Sci. Tech. Archaeol. Res.* **5**, 200–220 (2019).
9. G. Artioli, M. Secco, A. Addis, The Vitruvian legacy: Mortars and binders before and after the Roman world. *EMU Notes Miner.* **20**, 151–202 (2019).
10. F. Yang, B. Zhang, Q. Ma, Study of sticky rice– Lime mortar technology for the restoration of historical masonry construction. *Acc. Chem. Res.* **43**, 936–944 (2010).
11. C. Rodriguez-Navarro, E. Ruiz-Agudo, A. Burgos-Cara, K. Elert, E. F. Hansen, Crystallization and colloidal stabilization of $Ca(OH)_2$ in the presence of nopal juice (Opuntia ficus indica): Implications in architectural heritage conservation. *Langmuir* **33**, 10936–10950 (2017).
12. I. Villaseñor, E. Graham, The use of volcanic materials for the manufacture of pozzolanic plasters in the Maya lowlands: A preliminary report. *J. Archaeol. Sci.* **37**, 1339–1347 (2010).
13. A. Berman, L. Addadi, Å. Kvick, L. Leiserowitz, M. Nelson, S. Weiner, Intercalation of sea urchin proteins in calcite: Study of a crystalline composite material. *Science* **250**, 664–667 (1990).
14. S. Albeck, S. Weiner, L. Addadi, Polysaccharides of intracrystalline glycoproteins modulate calcite crystal growth in vitro. *Chem. A Eur. J.* **2**, 278–284 (1996).
15. J. Aizenberg, J. Hanson, T. F. Koetzle, S. Weiner, L. Addadi, Control of macromolecule distribution within synthetic and biogenic single calcite crystals. *J. Am. Chem. Soc.* **119**, 881–886 (1997).
16. B. Pokroy, A. N. Fitch, F. Marin, M. Kapon, N. Adir, E. Zolotoyabko, Anisotropic lattice distortions in biogenic calcite induced by intra-crystalline organic molecules. *J. Struct. Biol.* **155**, 96–103 (2006).
17. B. Pokroy, A. Fitch, E. Zolotoyabko, The microstructure of biogenic calcite: A view by high-resolution synchrotron powder diffraction. *Adv. Mater.* **18**, 2363–2368 (2006).
18. E. Zolotoyabko, Anisotropic lattice distortions in biogenic minerals originated from strong atomic interactions at organic/inorganic interfaces. *Adv. Mater. Interf.* **4**, 1600189 (2017).
19. M. Alberic, E. N. Caspi, M. Bennet, W. Ajili, N. Nassif, T. Azaïs, A. Berner, P. Fratzl, E. Zolotoyabko, L. Bertinetti, Y. Politi, Interplay between calcite, amorphous calcium carbonate, and intracrystalline organics in sea urchin skeletal elements. *Cryst. Growth Des.* **18**, 2189–2201 (2018).
20. Z. Deng, Z. Jia, L. Li, Biomineralized materials as model systems for structural composites: Intracrystalline structural features and their strengthening and toughening mechanisms. *Adv. Sci. (Weinh)* **9**, e2103524 (2022).
21. U. G. K. Wegst, H. Bai, E. Saiz, A. P. Tomsia, R. O. Ritchie, Bioinspired structural materials. *Nat. Mater.* **14**, 23–36 (2015).
22. D. Webster, The archaeology of Copán, Honduras. *J. Archaeol. Res.* **7**, 1–53 (1999).
23. K. Elert, E. Ruiz-Agudo, F. Jroundi, M. T. Gonzalez-Muñoz, B. W. Fash, W. L. Fash, N. Valentin, A. de Tagle, C. Rodriguez-Navarro, Degradation of ancient Maya carved tuff stone at Copan and its bacterial bioconservation. *npj Mater. Degrad.* **5**, 44 (2021).
24. J. J. De Yoreo, P. U. P. A. Gilbert, N. A. J. M. Sommerdijk, R. L. Penn, S. Whitelam, D. Joester, H. Zhang, J. D. Rimer, A. Navrotsky, J. F. Banfield, A. F. Wallace, F. M. Michel, F. C. Meldrum, H. Cölfen, P. M. Dove, Crystallization by particle attachment in synthetic, biogenic, and geologic environments. *Science* **349**, aaa6760 (2015).
25. J. Seto, Y. Ma, S. A. Davis, F. Meldrum, A. Gourrier, Y.-Y. Kim, U. Schilde, M. Sztucki, M. Burghammer, S. Maltsev, C. Jäger, H. Cölfen, Structure-property relationships of a biological mesocrystal in the adult sea urchin spine. *Proc. Natl. Acad. Sci. U.S.A.* **109**, 3699–3704 (2012).
26. Ö. Cizer, C. Rodriguez-Navarro, E. Ruiz-Agudo, J. Elsen, D. Van Gemert, K. Van Balen, Phase and morphology evolution of calcium carbonate precipitated by carbonation of hydrated lime. *J. Mater. Sci.* **47**, 6151–6165 (2012).
27. L. Addadi, S. Raz, S. Weiner, Taking advantage of disorder: Amorphous calcium carbonate and its roles in biomineralization. *Adv. Mater.* **15**, 959–970 (2003).
28. D. Gebauer, H. Cölfen, A. Verch, M. Antonietti, The multiple roles of additives in $CaCO_3$ crystallization: A quantitative case study. *Adv. Mater.* **21**, 435–439 (2009).
29. C. Rodriguez-Navarro, Ö. Cizer, K. Kudłacz, A. Ibañez-Velasco, C. Ruiz-Agudo, K. Elert, A. Burgos-Cara, E. Ruiz-Agudo, The multiple roles of carbonic anhydrase in calcium carbonate mineralization. *CrstEngComm* **21**, 7407–7423 (2019).
30. H. Li, H. L. Xin, D. A. Muller, L. A. Estroff, Visualizing the 3D internal structure of calcite single crystals grown in agarose hydrogels. *Science* **326**, 1244–1247 (2009).
31. A. S. Schenk, I. Zlotnikov, B. Pokroy, N. Gierlinger, A. Masic, P. Zaslansky, A. N. Fitch, O. Paris, T. H. Metzger, H. Cölfen, P. Fratzl, B. Aichmayer, Hierarchical calcite crystals with occlusions of a simple polyelectrolyte mimic complex biomineral structures. *Adv. Funct. Mater.* **22**, 4668–4676 (2012).
32. Y.-Y. Kim, K. Ganesan, P. Yang, A. N. Kulak, S. Borukhin, S. Pechook, L. Ribeiro, R. Kröger, S. J. Eichorn, S. P. Armes, B. Pokroy, F. C. Meldrum, An artificial biomineral formed by incorporation of copolymer micelles in calcite crystals. *Nat. Mater.* **10**, 890–896 (2011).
33. A. Lang, S. Mijowska, I. Polishchuk, S. Fermani, G. Falini, A. Katsman, F. Marin, B. Pokroy, Acidic monosaccharides become incorporated into calcite single crystals. *Chemistry* **26**, 16860–16868 (2020).
34. B. Xu, M. B. Toffolo, L. Regev, E. Boaretto, K. M. Poduska, Structural differences in archaeologically relevant calcite. *Anal. Methods* **7**, 9304–9309 (2015).
35. P. L. Chiang, Y. C. Tseng, H. J. Wu, S. H. Tsao, S. P. Wu, W. C. Wang, H. I. Hsieh, J. Y. Juang, Elastic moduli of avian eggshell. *Biology (Basel)* **10**, 989 (2021).
36. F. Jroundi, K. Elert, E. Ruiz-Agudo, M. T. Gonzalez-Muñoz, C. Rodriguez-Navarro, Bacterial diversity evolution in maya plaster and stone following a bio-conservation treatment. *Front. Microbiol.* **11**, 599144 (2020).
37. V. Presser, K. Gerlach, A. Vohrer, K. G. Nickel, W. F. Dreher, Determination of the elastic modulus of highly porous samples by nanoindentation: A case study on sea urchin spines. *J. Mater. Sci.* **45**, 2408–2418 (2010).
38. X. Fang, H. Bishara, K. Ding, H. Tsybenko, L. Porz, M. Höfling, E. Bruder, Y. Li, G. Dehm, K. Durst, Nanoindentation pop-in in oxides at room temperature: Dislocation activation or crack formation? *J. Am. Ceram. Soc.* **104**, 4728–4741 (2021).
39. D. Labonte, A.-K. Lenz, M. L. Oyen, On the relationship between indentation hardness and modulus, and the damage resistance of biological materials. *Acta Biomater.* **57**, 373–383 (2017).
40. M. E. Kunitake, L. M. Mangano, J. M. Peloquin, S. P. Baker, L. A. Estroff, Evaluation of strengthening mechanisms in calcite single crystals from mollusk shells. *Acta Biomater.* **9**, 5353–5359 (2013).
41. X. Li, Z.-H. Xu, R. Wang, In situ observation of nanograin rotation and deformation in nacre. *Nano Lett.* **6**, 2301–2304 (2006).
42. E. Doehne, C. A. Price, *Stone Conservation: An Overview of Current Research* (Getty Conservation Institute, 2010).
43. L. Straulino, S. Sedov, D. Michelet, S. Balanzario, Weathering of carbonate materials in ancient Maya constructions (Río Bec and Dzibanché): Limestone and stucco deterioration patterns. *Quat. Int.* **315**, 87–100 (2013).
44. K. R. Cho, Y.-Y. Kim, P. Yang, W. Cai, H. Pan, A. N. Kulak, J. L. Lau, P. Kulshershtha, S. P. Armes, F. C. Meldrum, J. J. De Yoreo, Direct observation of mineral–organic composite formation reveals occlusion mechanism. *Nat. Commun.* **7**, 10187 (2016).
45. M. Maldini, P. Montoro, S. Piacente, C. Pizza, ESI-MS, ESI-MS/MS fingerprint and LC-ESI-MS analysis of proathocyanidins from *Bursera simaruba* Sarg bark. *Nat. Prod. Commun.* **4**, 1671–1674 (2009).
46. A. B. Rodríguez-Navarro, P. Marie, Y. Nys, M. T. Hincke, J. Gautron, Amorphous calcium carbonate controls avian eggshell mineralization: A new paradigm for understanding rapid eggshell calcification. *J. Struct. Biol.* **190**, 291–303 (2015).
47. C. Rodriguez-Navarro, K. Elert, R. Ševčík, Amorphous and crystalline calcium carbonate phases during carbonation of nanolimes: Implications in heritage conservation. *CrstEngComm* **18**, 6594–6607 (2016).
48. H. M. Rietveld, A profile refinement method for nuclear and magnetic structures. *J. Appl. Cryst.* **2**, 65–71 (1969).
49. S. A. Markgraf, R. J. Reeder, High-temperature structure refinements of calcite and magnesite. *Am. Mineral.* **70**, 590–600 (1985).
50. J. Rodríguez-Carvajal, *Fullprof* (CEA/Saclay, 2001).
51. G. K. Williamson, W. H. Hall, X-ray line broadening from filed aluminium and wolfram. *Acta Metall.* **1**, 22–31 (1953).
52. W. C. Oliver, G. M. Pharr, An improved technique for determining hardness and elastic modulus using load and displacement sensing indentation experiments. *J. Mater. Res.* **7**, 1564–1583 (1992).
53. C. Merkel, J. Deuschle, E. Griesshaber, S. Enders, E. Steinhauser, R. Hochleitner, U. Brand, W. W. Schmahl, Mechanical properties of modern calcite-(*Mergerlia truncata*) and phosphate-shelled brachiopods (*Discradisca stella* and *Lingula anatina*) determined by nanoindentation. *J. Struct. Biol.* **168**, 396–408 (2009).
54. Z. Deng, H. Chen, T. Yang, Z. Jia, J. C. Weaver, P. D. Shevchenko, F. De Carlo, R. Mirzaeifar, L. Li, Strategies for simultaneous strengthening and toughening via nanoscopic intracrystalline defects in a biogenic ceramic. *Nat. Commun.* **11**, 5678 (2020).
55. A. P. Roberts, E. J. Garboczi, Elastic properties of model porous ceramics. *J. Am. Ceram. Soc.* **83**, 3041–3048 (2000).
56. K. L. Johnson, *Contact Mechanics* (Cambridge University Press, 2012).
57. H. H. Galicia-Aguilar, L. A. Rodríguez-González, C. M. Capetillo-Leal, R. Cámara-Sarmiento, A. J. Aguilar-Caballero, C. A. Sandoval-Castro, J. F. J. Torres-Acosta, Effects of *Havardia albicans* supplementation on feed consumption and dry matter digestibility of sheep and the biology of *Haemonchus contortus*. *Anim. Feed Sci. Technol.* **176**, 178–184 (2012).

58. E. Beniash, J. Aizenberg, L. Addadi, S. Weiner, Amorphous calcium carbonate transforms into calcite during sea urchin larval spicule growth. *Proc. R. Soc. Lond. B* **264**, 461–465 (1997).
59. K. M. Poduska, L. Regev, E. Boaretto, L. Addadi, S. Weiner, L. Kronik, S. Curtarolo, Decoupling local disorder and optical effects in infrared spectra: Differentiating between calcites with different origins. *Adv. Mater.* **23**, 550–554 (2011).
60. N. Floquet, D. Vielzeuf, V. Heresanu, D. Laporte, J. Perrin, Synchrotron high-resolution XRD and thermal expansion of synthetic Mg calcites. *Phys. Chem. Mineral.* **47**, 48 (2020).

Acknowledgments: We thank W.S. Fash, B. Fash, A. De Tagle, N. Valentin, the Instituto Hondureño de Antropología e Historia (IHAH), and the local Santander team at the Maya Sculpture Conservation Laboratory (LACEM) in Copan for help and continuous support, as well as for providing access to this archaeological Maya site and permit to sample historical plasters. We also thank the personnel of the Centro de Instrumentación Científica (CIC) of the University of Granada for help with TG/DSC, XRF, nanoindentation, FESEM, and TEM analyses. HRXRD experiments were performed at BL-04 MSPD beamline at ALBA Synchrotron with the collaboration of ALBA staff (F. Fauth). We also thank P. Alvarez for help during HRXRD analysis at ALBA. **Funding:** This work was funded by Santander Program for the Research and Conservation of Maya Sculpture, at the David Rockefeller Center for Latin American Studies (DRCLAS), Harvard University (to C.R.-N.); Spanish Government grant RTI2018-099565-B-I00 (to C.R.-N., E.R.-A., M.B.-R., K.E., and L.M.-G.); Spanish Government grant PID2021.125305NB.I00 funded by MCIN/ AEI /10.13039/501100011033 and by ERDF A way of making Europe (to C.R.-N., E.R.-A., M.B.-R., K.E., and L.M.-G.); Junta de Andalucía research group RNM-179 (to C.R.-N., K.E., and E.R.-A.); University of Granada, Unidad Científica de Excelencia UCE-PP2016-05 (to C.R.-N., K.E., and E.R.A.); and European Commission, H2020 Programme, Marie Skłodowska-Curie Action European Training network–Innovative Training Network (ETN-ITN), SUBlime (grant agreement #955986) (to C.R.-N., K.E., and E.R.-A.). **Author contributions:** Conceptualization: C.R.-N. and K.E. Methodology: C.R.-N., K.E., and E.R.-A. Investigation: M.B.-R., K.E., C.R.-N., L.M.-G., and E.R.-A. Writing (original draft): C.R.-N. Writing (review and editing): C.R.-N., K.E., E.R.-A., M.B.-R., and L.M.-G. **Competing interests:** The authors declare that they have no competing interests. **Data and materials availability:** All data needed to evaluate the conclusions in the paper are present in the paper and/or the Supplementary Materials.

Submitted 2 November 2022
Accepted 14 March 2023
Published 19 April 2023
10.1126/sciadv.adf6138

ScienceAdvances

Unveiling the secret of ancient Maya masons: Biomimetic lime plasters with plant extracts

Carlos Rodriguez-Navarro, Luis Monasterio-Guillot, Miguel Burgos-Ruiz, Encarnacin Ruiz-Agudo, and Kerstin Elert

Sci. Adv., **9** (16), eadf6138.
DOI: 10.1126/sciadv.adf6138

Science Advances (ISSN) is published by the American Association for the Advancement of Science. 1200 New York Avenue NW, Washington, DC 20005. The title *Science Advances* is a registered trademark of AAAS.